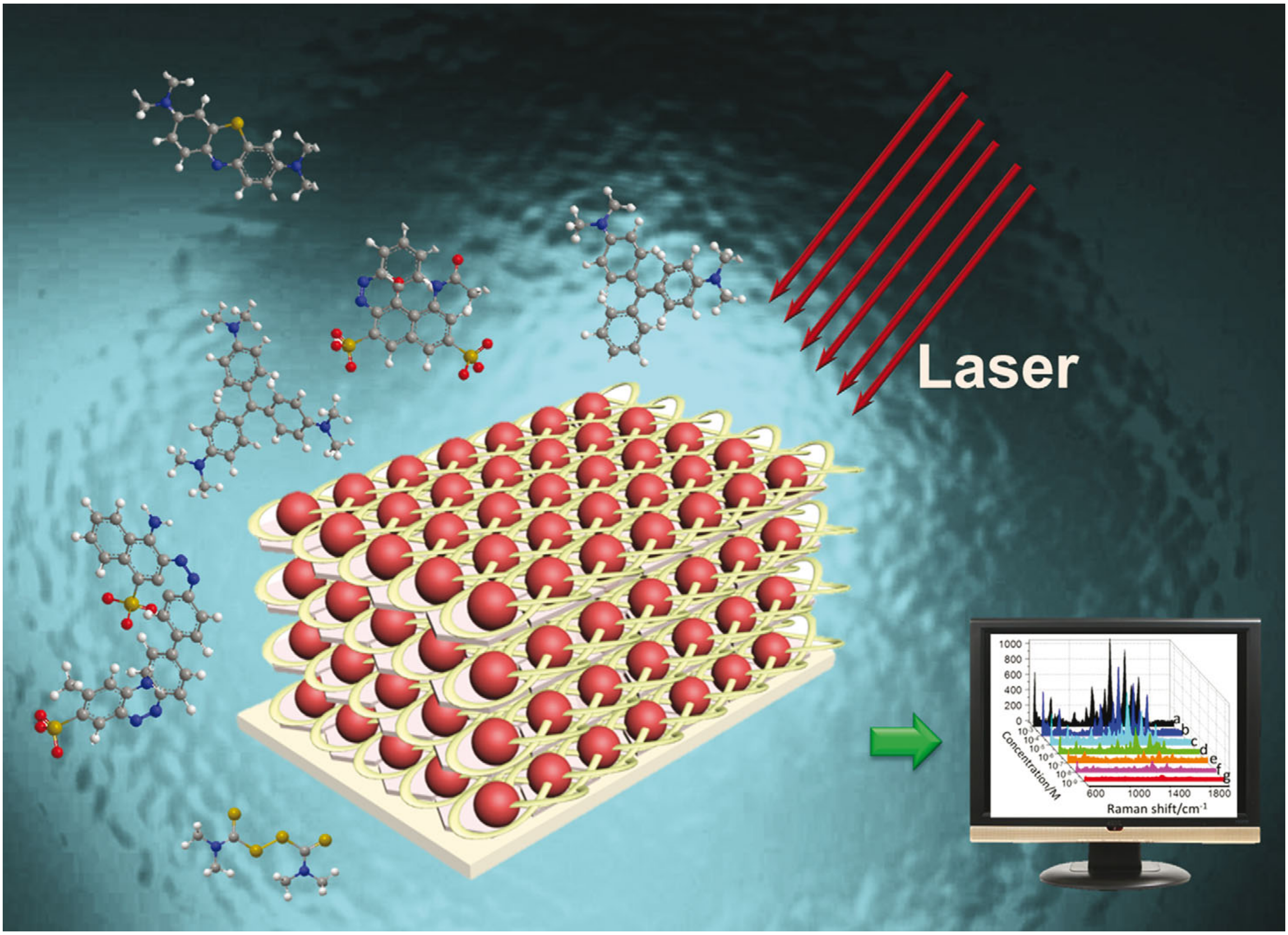

Highlighting work on a 2D surface enhanced Raman scattering (SERS) array presented by Prof. Dongpeng Yan, Prof. Min Wei and co-workers at the State Key Laboratory of Chemical Resource Engineering, Beijing University of Chemical Technology, Beijing, China.

Surface enhanced Raman scattering based on Au nanoparticles/layered double hydroxide ultrathin films

A two-dimensional SERS film based on Au nanoparticles and layered double hydroxide nanosheets has been fabricated, which shows an enhanced electromagnetic field and can be widely used in the detection of various analytes.

As featured in:

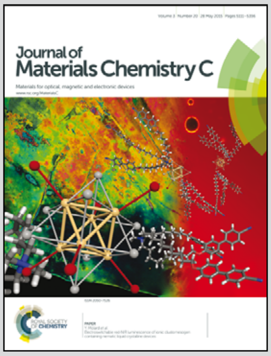

See Dongpeng Yan,
Min Wei *et al.*,
J. Mater. Chem. C, 2015, **3**, 5167.

ROYAL SOCIETY
OF **CHEMISTRY**

www.rsc.org/MaterialsC

Journal of
Materials Chemistry C

PAPER

View Article Online
View Journal | View Issue

Cite this: *J. Mater. Chem. C*, 2015, **3**, 5167

Surface enhanced Raman scattering based on Au nanoparticles/layered double hydroxide ultrathin films†

Rui Tian,[a] Mingwan Li,[a] Haiyan Teng,[a] Heng Luo,[a] Dongpeng Yan*[ab] and Min Wei*[a]

Received 27th November 2014,
Accepted 1st April 2015

DOI: 10.1039/c4tc02714k

www.rsc.org/MaterialsC

Surface-enhanced Raman scattering (SERS) is an effective characterization method which has shown broad applications in the field of detection and identification. In this work, we describe the facile fabrication of SERS ultrathin films (UTFs) based on a two-dimentional architecture *via* layer-by-layer assembly of hygroscopic sodium polyacrylate (PAAS) modified Au nanoparticles (NPs) and MgAl layered double hydroxide (LDH) nanosheets. The resulting Au@PAAS/LDH UTFs possess a periodic long-range ordered layered structure and dense immobilization of Au NPs within the LDH interlayer microenvironment. The distance of Au NPs in the x–y plane reaches as low as ∼2.16 nm, and thus the coupling of Au–Au NPs enabled an enhanced electromagnetic field and improved SERS effect. For example, a detection limit as low as 10^{-9} M could be obtained for Rhodamine 6G. Moreover, the obtained UTFs could be adapted to various solvents and dye molecules, confirming the versatility and the sensitivity of the 2D UTFs. In addition, the UTF exhibits satisfactory reusability and high stability at high temperature and various pH values. Therefore, this work highlights a high-efficiency SERS film material with facile preparation, which guarantees their further application in environmental detection and analysis.

1 Introduction

Surface-enhanced Raman scattering (SERS) is an ultrasensitive spectroscopic characterization technique, which has been widely used in label-free detection and identification of pollutants, biomolecules, and chemical residues.[1–5] The properties of SERS-active materials play a key role in determining the SERS sensitivity and effectiveness, which have been regarded as the research focus in this field.[6,7] Conventional SERS-active materials can be classified into two categories: metallic nanoparticles (NPs) in a colloidal solution (such as Au, Ag and Cu)[8,9] and roughened metallic surfaces (*e.g.*, films fabricated through electron beam lithography, chemical etching, mechanical deformation and electroplating).[10,11] However, the former often suffers from the formation of large conglomerations of NPs, while the latter has been limited by the complicated fabrication process and unstable nature of the nanoparticles.[12] Therefore, the development of suitable species and/or new approaches toward the facile fabrication of Raman-active materials with the advantages of distinct signals, good reproducibility and high stability in the surrounding medium remains a challenging goal.[1,13–15]

Au NP is a well-known SERS-active medium, which has promising applications in the field of detection and analysis.[16,17] To achieve high SERS signal and sensitivity, control over ordered degree and uniform particle distribution of Au NPs is of crucial importance,[1,18–20] as a result of the NP–NP couplings.[21,22] To meet this requirement, one effective way is to assemble Au NPs with a suitable solid building block to obtain an ordered structure and morphology, and an idealized building block can also be regarded as an effective nano-spacer for efficient NP–NP couplings in both horizontal and vertical directions.[23,24] Layered double hydroxides (LDHs), with the general formula of $[\mathrm{M^{II}}_{1-x}\mathrm{M^{III}}_{x}(\mathrm{OH})_2]^{z+}\mathrm{A}^{n-}{}_{z/n}\cdot y\mathrm{H_2O}$ ($\mathrm{M^{II}}$ and $\mathrm{M^{III}}$ are di- and trivalent metal ions respectively, and A^{n-} is a guest anion), are one family of inorganic layered matrix with tunable versatility in chemical composition and high stability.[25–31] Recently, the exfoliated LDH nanosheet has been applied as a building block for the fabrication of various multifunctional thin films with advanced performance.[32,33] In our previous work, we reported several LDH nanosheet-based materials for fluorescence imaging,[34] intelligent display[35] and optical detection applications.[36] The confined environment imposed by the 2D LDH nanosheets usually affords the as-prepared films

---

[a] State Key Laboratory of Chemical Resource Engineering, Beijing University of Chemical Technology, Beijing 100029, P. R. China. E-mail: yandongpeng001@163.com, weimin@mail.buct.edu.cn; Fax: +86-10-64425385; Tel: +86-10-64412131

[b] Key Laboratory of Theoretical and Computational Photochemistry, Ministry of Education, College of Chemistry, Beijing Normal University, Beijing 100875, China

† Electronic supplementary information (ESI) available: Morphology of Au NPs; assembly process and morphological characterization of $(\mathrm{Au@PAAS/LDHs})_n$ (n = 0–10) UTFs; Raman tests of LDH nanosheets and drop-casted samples; loading and unloading properties of the UTFs. See DOI: 10.1039/c4tc02714k

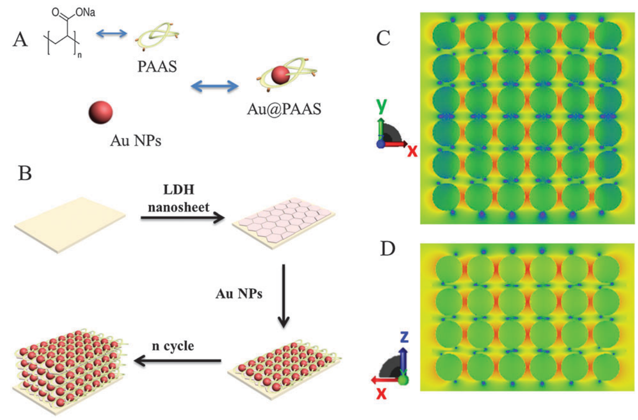

Scheme 1 (A) Preparation of a Au@PAAS precursor; (B) schematic representation of the assembly process; (C) and (D) are the finite-difference time-domain (FDTD) simulation in *x*–*y* and *x*–*z* planes.

with superior performance compared with the pristine solution and solid forms. This thus inspires us to fabricate a new type of 2D-organized SERS-active material *via* the assembly of Au NPs with LDH nanosheets, which may take advantages of both components: (i) vertically and horizontally dense immobilization of Au NPs can be achieved *via* the layer-by-layer assembly approach, in which the short distance between Au NPs would promote the formation of "hotspots";[37,38] (ii) the incorporation of Au into the rigid LDH matrix would provide a high stability and reusability so as to perform highly-efficient SERS detection.

In this work, we demonstrate the fabrication of $(Au@PAAS/LDH)_n$ ultrathin films *via* a two-step procedure (Scheme 1): (1) modification of Au NPs (particle size: 14 nm) with hygroscopic sodium polyacrylate (PAAS) to obtain Au@PAAS; (2) assembly of Au@PAAS with positively-charged LDH nanosheets *via* a layer-by-layer method to obtain $(Au@PAAS/LDH)_n$ UTFs. The as-prepared UTFs display a periodic long-range ordered structure and dense immobilization of Au NPs within the LDH interlayer microenvironment. The distance between adjacent Au NPs can reach as short as 2.16 nm in the horizontal direction (Scheme 1B), which results in a largely enhanced electromagnetic field. The vibration of molecules in this electromagnetic field can be further amplified, which provided a detection limit of Rhodamine 6G (R6G) as low as 10^{-9} M. Moreover, these UTFs can be adapted in the detection and identification for various solvents and analytes. In addition, largely-improved reusability and remarkable stability can also be achieved for these sophisticated UTFs. Therefore, a facilely fabricated SERS material with finely tuned uniformity and high coupling between particles can be obtained, which realizes the optimized electromagnetic field enhancement, and guarantees their further application in the fields of real-time and on-site detection.

2 Experimental section

Materials

Hydrogen tetrachloroaurate hydrate ($HAuCl_4 \cdot 3H_2O$, >99.9%) was purchased from Aldrich Co. Ltd. Analytical-grade chemicals including formamide, $Mg(NO_3)_2 \cdot 6H_2O$, $Al(NO_3)_3 \cdot 9H_2O$, urea, sodium citrate, sodium polyacrylate (PAAS), $NaNO_3$ and HNO_3 were purchased from Aladdin Chemical. Co. Ltd. Deionized and de-CO_2 water was used in all the experimental processes.

Preparation of Au NPs

The aqueous synthesis of sodium citrated reduced Au NPs was performed according to a reported method.[39,40] In a typical synthesis, 100 ml of $HAuCl_4 \cdot 3H_2O$ (1.0 mmol) was heated to boiling under stirring, followed by addition of 10 ml of sodium citrate (38.8 mmol). The solution was stirred under boiling for 10 min, and at room temperature for another 10 min. The obtained Au NP colloidal suspension was cooled to room temperature and stored at 4 °C.

Fabrication of $(Au@PAAS/LDH)_n$ UTFs

The process of synthesis and exfoliation of MgAl-LDH was similar to the procedure described in our previous work.[34,35] 0.1 g of MgAl-LDH was shaken in formamide (100 ml) for 24 h to produce a colloidal suspension of exfoliated MgAl-LDH nanosheets.[41] The quartz glass substrate was cleaned by immersion in a concentrated H_2SO_4–30% H_2O_2 (7 : 3, v/v) solution for 30 min. The Au@PAAS solution was obtained by adding PAAS (0.5 g L^{-1}, 2 ml) solution into an Au NP colloid solution (8 ml). In order to fabricate the $(Au@PAAS/LDH)_n$ films, the substrate was dipped in a colloidal suspension (1 g L^{-1}) of LDH nanosheets for 10 min followed by washing thoroughly, and then immersed into the Au@PAAS solution for another 10 min. Multilayer films of $(Au@PAAS/LDH)_n$ were fabricated by alternate deposition of LDH nanosheets and Au@PAAS aqueous solution for *n* cycles. Finally, the UTFs were rinsed and washed thoroughly with deionized water and dried in a flow of nitrogen gas.

Loading and unloading of analytes

Taking Rhodamine 6G (R6G) as the example for Raman reporter, the UTFs were dipped into an R6G solution (pH = 10) for 2 h to load dyes onto UTFs for Raman test, and the unloading process was carried out by dipping the UTFs into water (pH = 10) for another 2 h.

Sample characterization

Transmission electron microscopy (TEM) images were recorded on a JEOL JEM-2100 TEM with an accelerating voltage of 200 kV. The UV-vis absorption spectra were collected on a Shimadzu U-3000 spectrophotometer, with a slit width of 1.0 nm. X-ray diffraction patterns (XRD) of the UTFs were recorded using a Rigaku 2500 VB2 + PC diffractometer under the conditions: 40 kV, 50 mA, Cu K_α radiation (λ = 0.154056 nm) with step-scanned in steps of 0.04° (2θ) in the range from 0.5° to 2° using a count time of 10 s per step. The morphology of thin films was investigated using a scanning electron microscope (SEM Hitachi S-3500), and the accelerating voltage applied was 20 kV. The surface roughness data were obtained using a NanoScope IIIa atomic force microscope (AFM) from Veeco Instruments. The SERS measurements were performed at room temperature on a LabRAM ARAMIS Raman system using a 633 nm helium–neon laser line as the excitation source. The laser spot size was ~1 μm with an incident power of 0.325 mW and an acquisition time of 1 s. The light impinging on the multilayer structures is propagating along *z* and polarized in the *x* direction. The accumulation time and laser power were the same for all Raman spectra. The fluorescence spectra were performed on a RF-5301PC fluorospectrophotometer with an excitation wavelength of 500 nm. The fluorescence emission spectra range from 520–650 nm, and both the excitation and emission slits are set to be 10 nm.

3 Results and discussion

Assembly of the $(\mathrm{Au@PAAS/LDH})_n$ UTFs

The well-dispersed Au NP colloidal suspension with a particle size of 14 nm can be synthesized by the reduction of a $HAuCl_4$ solution (Fig. S1 in ESI†), and a typical absorption band at 520 nm is observed as a result of plasmon resonance (Fig. S2, ESI†).[39] An attempt for the direct assembly of Au NPs with LDH nanosheets was carried out firstly, but a serious aggregation and non-uniform distribution of Au NPs are observed (Fig. S3, ESI†). Alternatively, Au NPs were firstly modified with PAAS to obtain Au@PAAS with a better dispersion, which was further used to assemble with LDH nanosheets *via* a layer-by-layer method. The multilayer assembly process of the $(\mathrm{Au@PAAS/LDH})_n$ UTFs was monitored by UV-vis absorption spectroscopy. As PAAS shows no absorption (Fig. S3, ESI†), the absorption band at ~520 nm is attributed to plasmon resonance absorption of Au NPs in the UTFs (Fig. 1A). The band intensity increases linearly with the increase of bilayer number *n* (Fig. 1C), indicating a stepwise and regular film growth procedure, which can be further confirmed by the visible color evolution (Fig. 1B). Moreover, the initial molar ratio of Au NPs to PAAS was carefully studied, and the typical UV-vis spectra for $(\mathrm{Au@PAAS/LDH})_{10}$ UTFs with variable Au/PAAS ratios are displayed in Fig. S4 (ESI†). It shows that the absorbance increases linearly with the increasing ratio of Au/PAAS, suggesting that the quantity of assembled Au NPs could be finely tuned within the UTF, which may further tailor the related electromagnetic field around Au NPs.

The structural and morphological studies of the $(\mathrm{Au@PAAS/LDHs})_n$ UTFs

The structural and morphological properties of $(\mathrm{Au@PAAS/LDHs})_n$ UTFs were further studied. The small angle XRD pattern (Fig. 2A) displays a basal reflection at $2\theta = 0.525°$, indicating a periodic long-range ordered superlattice structure with a repeating thickness of 16.81 nm. The obtained spacing distance is close to the monolayer arrangement of Au NPs (14 nm) in the interlayer region of LDH nanosheets (0.48 nm). In this way, a thin and rigid LDH nanosheet is employed as a confined nanospacer between Au NPs in the adjacent layers and the distance between Au NPs in the vertical direction can be estimated to be ~2.8 nm (Scheme 1B). The typical top-view SEM images of these UTFs (Fig. 2B and Fig. S5, ESI†) reveal a homogeneous and uniform surface morphology. The NPs exhibit dense immobilization and uniform arrangement in the *x*–*y* plane, and the average distances are about 84.5, 53.1, 35.9, 21.2, 9.5 and 2.16 nm between adjacent Au NPs as the Au : PAAS ratio ranges from 0.25 to 4 as shown in TEM images (Fig. S6, ESI†). The obtained structure may facilitate the formation of "hotspots" which is beneficial to their coupling for the enhancement of the near-field intensity. The AFM topographical images (2 μm × 2 μm) of the $(\mathrm{Au@PAAS/LDHs})_n$ UTFs are illustrated in Fig. 2C and Fig. S7 (ESI†), in which the well-dispersed Au NPs are observed with a high density. The root-mean square (RMS) roughness ranges from 3.60–10.26 nm (Table S1, ESI†), indicating the continuous and smooth surface of these UTFs. The UTF thickness can be estimated based on their side-view SEM images (Fig. 2D and Fig. S8, ESI†), from which an approximately linear increase of film thickness as a function of *n* was observed. An average thickness increment of 16.40 nm per bilayer cycle was obtained (Table S1, ESI†), which is consistent with the XRD observations (16.81 nm). The results further confirm the uniform and periodic layered structure of these UTFs throughout the fabrication process.

SERS performances

The field enhancement of $(\mathrm{Au@PAAS/LDH})_n$ UTFs was further studied by detecting their Raman intensity. In this work, R6G, which possesses well-established vibrational features (Table S2, ESI†), was employed as the target analyte. The laser line of 633 nm which does not disturb the fluorescence of R6G was

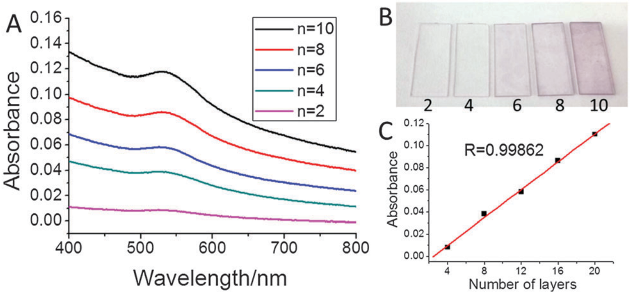

Fig. 1 (A) UV-vis absorption spectra, (B) photographs, and (C) linear correlation between absorbance at 520 nm and number of layers for the $(\mathrm{Au@PAAS/LDHs})_n$ (n = 0–10) UTFs (the molar ratio of Au : PAAS is 4 : 1).

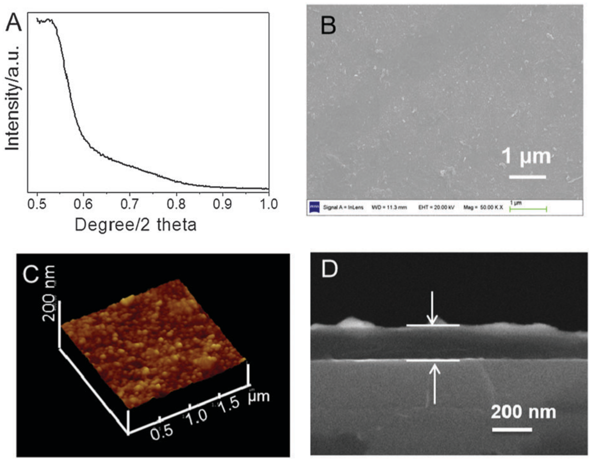

Fig. 2 The structural and morphological characterization of $(\mathrm{Au@PAAS/LDH})_{10}$ UTF: (A) XRD pattern, (B) top-view SEM image, (C) tapping-mode AFM topographical image, and (D) side-view SEM image.

chosen for all the SERS measurements. The Raman spectrum of $(Au@PAAS/LDH)_{10}$ UTF was recorded (Fig. S9, ESI†), which shows relatively weak vibrational peaks compared with that of R6G. Fig. S10 (ESI†) displays the Raman signals of polar light irradiated from different polarization directions. It is found that the Raman signals from various directions show equivalent intensity at 609, 1310, 1360 and 1649 cm^{-1}, respectively, which indicates that the LDH nanosheets have no influence on SERS performance of Au NPs. As a result, LDH nanosheets serve as a favorable matrix for the good dispersion and regular stacking of Au NPs for the investigation of the near-field enhancement effect. Moreover, $(Au@PAAS/LDH)_n$ UTFs with various Au/PAAS molar ratios were further studied (Fig. 3). Compared with the bare Au NPs on substrates which exhibit low SERS effect and inhomogeneity (Fig. S11, ESI†), the increase of the Au/PAAS molar ratio has effectively promoted the Raman intensity. Raman mapping in Fig. 3 indicated that good uniformity can be obtained for a ratio of 2 to 4. Thus, UTF with Au/PAAS ratio of 4 : 1 possesses better near-field enhancement effect and SERS signal, and the good uniformity enabled its practical use for subsequent tests.

Raman signals of R6G (10^{-3} M) over the $(Au@PAAS/LDH)_n$ UTFs were studied in comparison with that of the bare glass substrate. Notable enhancement of the Raman signals of R6G is observed on the UTFs, and the signal intensities with R6G loaded on $(Au@PAAS/LDH)_{10}$ UTF were ~200 times stronger than those obtained on glass (Fig. S12, ESI†). In the study of SERS performance for the $(Au@PAAS/LDH)_n$ UTFs with a single layer ($n = 1$) and multilayer ($n > 1$), the multilayer ($n = 10$) UTF exhibited much more enhanced intensity (Fig. S13, ESI†) due to the accumulated signal. In addition, to quantitatively measure the enhancement capability of the $(Au@PAAS/LDH)_{10}$ UTF, SERS spectra for the UTF treated with various R6G solutions (concentration: from 10^{-3} M to 10^{-9} M) were recorded (Fig. 4). The detection limit in the $(Au@PAAS/LDH)_n$ UTF system can reach as low as 10^{-9} M, which shows a significant promotion for detection compared with the pure glass substrate (10^{-3} M). Such a low detection limit can be related to the enhanced electromagnetic field induced by the plasmonic couplings of densely arranged Au NPs in the vertical direction. And this detection limit is slightly higher or comparable with those of the previous reported systems for the detection of R6G by Au NPs (10^{-8} M to 10^{-9} M).[42–46]

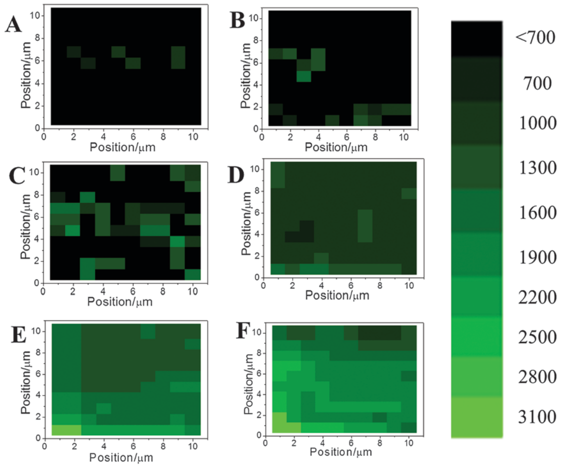

Fig. 3 Raman mapping of UTFs with various Au/PAAS molar ratios: (A) Au : PAAS = 0.25 : 1, (B) Au : PAAS = 0.5 : 1, (C) Au : PAAS = 1 : 1, (D) Au : PAAS = 2 : 1, (E) Au : PAAS = 3 : 1, (F) Au : PAAS = 4 : 1.

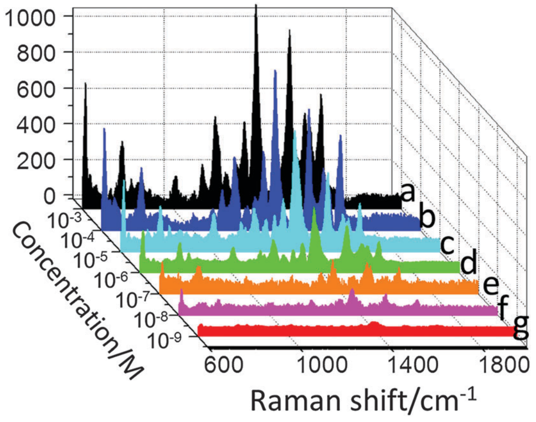

Fig. 4 SERS spectra of R6G with various concentrations over $(Au@PAAS/LDH)_{10}$ UTF: (a) 10^{-3} M, (b) 10^{-4} M, (c) 10^{-5} M, (d) 10^{-6} M, (e) 10^{-7} M, (f) 10^{-8} M and (g) 10^{-9} M.

A 3D finite-difference time-domain (FDTD) simulation was adopted by a commercial FDTD package (EMpro 2011.07) to study the spatial distribution of the electric fields, and a laser wavelength of 633 nm propagates along the z direction and polarized in the x direction. With Au–Au distances about 2.16 nm in the x–y plane and 2.8 nm for the x–z cross section, regular 'hot spots' between the neighboring Au NPs in the x–y plane and a certain degree of enhancement in the x–z cross section can be observed (Scheme 1C and D and Fig. S14, ESI†).[47,48] The abundant 'hot spots' in the x–y plane may be responsible for the sensitive SERS detection of analytes. Moreover, several factors would influence the distribution of induced dipoles and electromagnetic field, such as the direction of polarization light, total size of the nano array, distance and coupling effect between adjacent nanoparticles.[49–51] From this viewpoint, we investigated the effect of coupling from adjacent nanoparticles, considering both the incident light and the intense field induced by the surrounding nanoparticles (Fig. S15 and S16, ESI†). It is found that the asymmetric arrangement of nanoparticles in the x or y direction induces an inhomogeneous field distribution; while a more uniform distribution is obtained by adding nanoparticles in the boundary or extending the size of the nano array.

The local EM enhancement factors is estimated to be ~9.38×10^4, roughly as the fourth power of the local field: $G_{\text{loc}} = [E_{\text{loc}}(\lambda)/E_0(\lambda)]^4$.[52–54] In addition, the experimental enhancement factor has also been calculated based on the reported expression: $G = (I_{\text{SERS}}/I_{\text{Raman}}) \times (N_{\text{Raman}}/N_{\text{SERS}})$, where I_{SERS} and I_{Raman} are the Raman signal intensity in the SERS spectra and blank Raman spectra; N_{Raman} and N_{SERS} are the number of molecules in the range of the laser spot area.[55]

Therefore, the value of I_{SERS}/I_{Raman} is about 200 at 1508 cm^{-1} as displayed in Fig. S12 (ESI†), and N_{Raman} and N_{SERS} are supposed to be 0.945×10^8 and 0.802×10^6 in the volume of laser spot.[56,57] Accordingly, the EF of (Au@PAAS/LDH)$_{10}$ UTF is $\sim 2.36 \times 10^4$, which is in accordance with the calculated EF ($\sim 9.38 \times 10^4$). Therefore, the (Au@PAAS/LDH)$_{10}$ UTF possesses strong electric fields at the nanogaps between Au NPs, and can be used in SERS applications.

Application in the detection of various analytes

In actual cases, various analytes are often dispersed in different media (such as organic and aqueous solutions). This situation requires a versatile sensor toward various analytes in the aqueous or organic phase. In this regard, the application scope of (Au@PAAS/LDH)$_{10}$ UTF was further studied in several typical solvents (acetone, formamide, 1,2-dichloroethane (DCE), ethanol and water) and toward different analytes (methylene blue, congo red, crystal violet, acid red and nile blue). Fig. 5A shows the SERS performance of R6G in different solvents, whose vibrational peaks (609, 770, 1310, 1360, 1508 and 1649 cm^{-1}) are clearly detected for all these samples. Moreover, to identify the versatility and the sensitivity of the UTFs, several analytes were also detected. Taking methylene blue as an example, Raman peaks at 448, 1188, 1397 and 1627 cm^{-1} are observed as typical vibration for the drop-casted sample on glass (Fig. S17A, ESI†). A concentration down to 10^{-9} M can be measured by the (Au@PAAS/LDH)$_{10}$ UTF with obvious Raman vibration peaks from methylene blue (Fig. 5B). Furthermore, congo red, crystal violet, acid red and nile blue are detected as well (the reference sample (*ca.* 10^{-2} M) fabricated by a drop-casting method are shown in Fig. S17B–E, ESI†). Their detection limit values are 10^{-9} M for congo red, 10^{-10} M for crystal violet, 10^{-4} M for acid red and 10^{-10} M for nile blue, respectively (Fig. 5C–F). Therefore, the application range of (Au@PAAS/LDH)$_n$ UTFs can be readily extended to various analytes regardless of molecular binding; particularly, the conjugated molecules containing C=C bonds, aromatic rings and/or heterocyclic rings may provide a better signal and lower detection limit due to their strong Raman vibration.

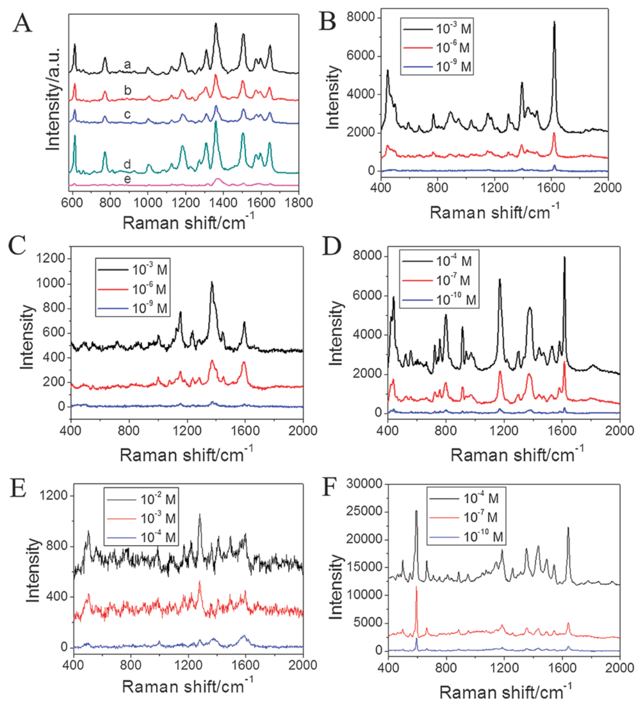

Fig. 5 (A) SERS spectra for the (Au@PAAS/LDH)$_{10}$ UTF treated with R6G (10^{-3} M) in different solvents ((a) ethanol, (b) water, (c) dichloroethane, (d) formamide, (e) acetone); SERS detection toward various analytes with different concentrations: (B) methylene blue, (C) congo red, (D) crystal violet, (E) acid red, (F) nile blue.

To further extend the Au@PAAS/LDH towards SERS application in real analyte systems, the SERS performance of (Au@PAAS/LDH)$_{10}$ has also been analysed for the typical chemical residues in food. Fishery antiseptics (malachite green, a forbidden antiseptic in the seafood industry) and ectoparasiticide (thiram, a commonly ectoparasiticide in seed and crop) have been taken as examples. Fig. S18A (ESI†) shows the Raman characteristic vibration of thiram powder, and vibration bands at 395, 560, 928 and 1380 cm^{-1} can be assigned to the characteristic stretching of S–S, S=S, C=S and C–N, respectively. SERS measurement of different concentrations of thiram in a mixture of water and formamide by (Au@PAAS/LDH)$_{10}$ UTF has been shown in Fig. 6A, in which the 10^{-7} M can be detected for this stable UTF. This detection limit is almost the same as the previous reported values.[58–61] Moreover, SERS measurements for malachite green were also performed and a concentration down to 10^{-12} M can be detected (Fig. 6B), in which the characteristic vibration bands are located in the same positions as the powdered form (Fig. S18B, ESI†). This result is much lower than the general detection limit in previous literature.[62–65] Therefore, these (Au@PAAS/LDH)$_n$ UTFs can be readily extended to other systems for the detection of low-concentration chemical residues, which may pave an effective way for real SERS application.

Moreover, the dye molecules (such as R6G) are also one of the most common chemical residues in real systems, such as in paints. Herein, the trace detection of the R6G dye used in paints has been further studied. Fig. 7 shows the detailed procedure and the Raman spectrum detected in this real application. After dissolving the R6G in paints in water and loading it using (Au@PAAS/LDH)$_{10}$ UTF, the characteristic Raman shifts assigned to R6G at 609, 770, 1310, 1360, 1508 and 1640 cm^{-1} can be clearly observed. Therefore, this Au@PAAS/LDH system can be potentially used for the trace detection of residues in the printing and dyeing fields.

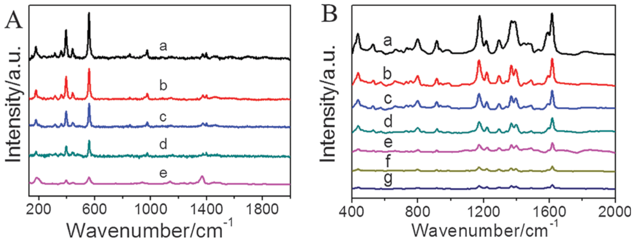

Fig. 6 SERS detection toward chemical residue analytes with different concentrations: (A) thiram ((a) 10^{-3} M, (b) 10^{-4} M, (c) 10^{-5} M, (d) 10^{-6} M and (e) 10^{-7} M), and (B) malachite green ((a) 10^{-6} M, (b) 10^{-7} M, (c) 10^{-8} M, (d) 10^{-9} M, (e) 10^{-10} M, (f) 10^{-11} M and (g) 10^{-12} M).

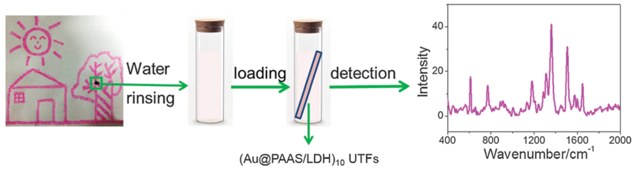

Fig. 7 The detailed procedure of R6G detection in paints, and the obtained Raman spectrum by SERS of (Au@PAAS/LDH)$_{10}$ UTF.

Reusability and stability tests

If the Au@PAAS/LDH UTF has the ability to load/unload analytes in a controlled fashion, the serious problem for traditional solid-state SERS materials—irreversible binding of the substrate with the analyte—can be avoided. And the loaded analyte can be concentrated in the interlayer of LDH due to the confinement effect.[66,67] After the (Au@PAAS/LDHs)$_{10}$ UTF was immersed in an R6G solution (pH = 10) to load the dye for Raman test, pure water was used to rinse the UTF to remove the excess R6G from the surface. The aim of this operation is to ensure the loaded R6G is incorporated into the UTF at the ''hotspot'' formed by adjacent Au NPs. The fluorescence emission spectra of the dye-loaded UTF reveal a strong emission at ~550 nm (Fig. 8A) originating from the luminescence of R6G. Comparison on the fluorescence spectra of (Au@PAAS/LDH)$_{10}$, (Au/LDH)$_{10}$ and (PAAS/LDH)$_{10}$ UTF shows that the employment of PAAS enables the quantitative loading of R6G into the UTF, while UTF without PAAS cannot capture the R6G molecules in the aqueous solution effectively (Fig. S19, ESI†). Additionally, release of the incorporated R6G was measured by the release kinetics of R6G in water at pH = 10 (Fig. S20 and S21, ESI†), indicating a complete unloading process. The complete loading and unloading process can also be verified by SERS measurements before and after loading of R6G (Fig. 8B) with the obviously observed vibrations at characteristic bands. The reversible tests were also carried out in different solvents (acetone, formamide, DCE and ethanol) containing R6G. The results reveal that these organic solvents are suitable for the loading and partial unloading of R6G; while water (pH = 10) can achieve an almost complete release of R6G within the UTF (Fig. 8C). Reusability, which is a key factor in practical applications,[36] was also demonstrated by immersing the UTF in an R6G solution and water (pH = 10) alternatively (Fig. 8D). And the complete loading and unloading process for six cycles can be observed, which is in accordance with reversible adsorption behavior in polyelectrolyte LbL films.[68–71] Therefore, addition of PAAS into Au NPs can effectively capture the low-concentration analytes into the interlayer environment of LDHs in a reversible manner.

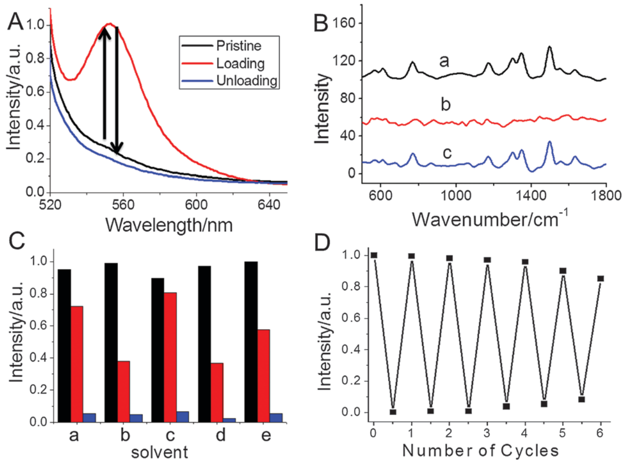

Fig. 8 Reversibility test of (Au@PAAS/LDH)$_{10}$ UTF: (A) relative fluorescence emission spectra, (B) SERS measurements ((a) loading, (b) unloading, (c) reloading), (C) relative fluorescence intensity of R6G in different solvents ((a) acetone, (b) formamide, (c) DCE, (d) water, (e) ethanol; black: loading in the solvent, red: unloading in the solvent, blue-unloading in water at pH = 10), and (D) fluorescence intensity of the Au@PAAS/LDH UTF treated by an R6G solution and H_2O alternatively.

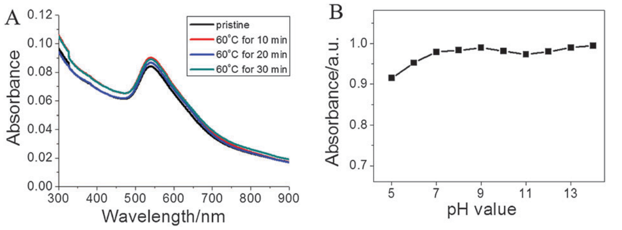

Fig. 9 Stability test of the (Au@PAAS/LDH)$_{10}$ UTF recorded by UV-vis absorption spectra: (A) heat treatment at 60 °C for various times, and (B) absorbance at 520 nm at different pH values.

The morphology change of the (Au@PAAS/LDHs)$_{10}$ UTF was monitored by AFM images during a complete loading–unloading process. The original UTF surface (Fig. S22A, ESI†) is smooth with a RMS roughness of 9.7 nm, while a relative rough surface is observed after loading of R6G (Fig. S22B, ESI†), accompanied with an increase in RMS roughness (12.6 nm). After unloading R6G using water, a relatively smooth surface is recovered with a RMS roughness of 10.1 nm (Fig. S22C, ESI†). The reversible changes in morphology indicate that the embedding and removal of R6G impose no obvious influence on the structure of (Au@PAAS/LDHs)$_n$ UTF.[72]

The stability of the obtained (Au@PAAS/LDH)$_{10}$ UTF was further studied by monitoring its UV-vis spectrum at elevated temperature and various pH values. Upon heating the (Au@PAAS/LDH)$_{10}$ UTF at 60 °C from 0 to 30 min, a slight decrease in absorption intensity at ~520 nm is observed without red-shift or broadening (Fig. 9A). This phenomenon demonstrated that high temperature did not cause the oxidation or aggregation of Au NPs, which may be attributed to the protection of LDH nanosheets.[33,34] Similar results are also obtained when the UTFs are treated with different pH values (Fig. 9B): no significant change in absorbance at ~520 nm is observed, indicating that the (Au@PAAS/LDH)$_{10}$ UTF remains stable in the pH range 5–14.

4 Conclusions

In summary, ordered (Au@PAAS/LDH)$_n$ UTFs were fabricated by a facile assembly of inorganic LDH nanosheets with sodium polyacrylate (PAAS) modified Au NPs on quartz substrates. The UTFs exhibit a periodic long-range heterogeneous structure and uniform morphology. Tight arrangement of Au NPs with about 2.16 nm and 2.8 nm in *x*–*y* and *x*–*z* planes can be constructed using LDH nanosheets, giving rise to an enlarged electromagnetic field for SERS detection. The concentrated dye molecules in the $(Au@PAAS/LDH)_n$ UTFs can be influenced by the generated electromagnetic field, and a concentration down to 10^{-9} M for R6G could be successfully detected due to the intensified vibration of molecules. This system was also studied for different solvents (acetone, formamide, 1,2-dichloroethane (DCE), ethanol and water) and various dye molecules (methylene blue, congo red, crystal violet, acid red, nile blue, thiram and malachite green), further confirming the versatility of the UTFs. Moreover, the as-prepared UTFs exhibit decent reusability and stability at high temperature and various pH values, which guarantees their practical recycling applications. Therefore, it is anticipated that this facile and cost-effective strategy for fabrication of near-field enhanced materials would facilitate potential applications in the detection and identification of the commonly used analyte molecules.

Acknowledgements

This work was supported by the 973 Program (Grant No. 2014CB932104), the National Natural Science Foundation of China (NSFC), Beijing Municipal Natural Science Foundation (Grant No. 2152016), and the Fundamental Research Funds for the Central Universities (YS1406). M. Wei appreciates the financial aid from the China National Funds for Distinguished Young Scientists of the NSFC.

Notes and references

1 M. P. Cecchini, V. A. Turek, J. Paget, A. A. Kornyshev and J. B. Edel, *Nat. Mater.*, 2013, **12**, 165.

2 R. Jin, Y. C. Cao, C. S. Thaxton and C. A. Mirkin, *Small*, 2006, **2**, 375.

3 V. Guieu, F. Lagugne-Labarthet, L. Servant, D. Talaga and N. Sojic, *Small*, 2008, **4**, 96.

4 T. Schmid, L. Opilik, C. Blum and R. Zenobi, *Angew. Chem., Int. Ed.*, 2013, **52**, 5940.

5 D. Graham, *Angew. Chem., Int. Ed.*, 2010, **49**, 9325.

6 W. E. Doering, M. E. Piotti, M. J. Natan and R. G. Freeman, *Adv. Mater.*, 2007, **19**, 3100.

7 P. Wang, O. Liang, W. Zhang, T. Schroeder and Y. H. Xie, *Adv. Mater.*, 2013, **25**, 4918.

8 B. Liu, G. Han, Z. Zhang, R. Liu, C. Jiang, S. Wang and M. Y. Han, *Anal. Chem.*, 2012, **84**, 255.

9 A. Mezni, I. Balti, A. Mlayah, N. Jouini and L. S. Smiri, *J. Phys. Chem. C*, 2013, **117**, 16166.

10 Y. J. Oh and K. H. Jeong, *Adv. Mater.*, 2012, **24**, 2234.

11 C. C. Chang, K. H. Yang, Y. C. Liu, T. C. Hsu and F. D. Mai, *ACS Appl. Mater. Interfaces*, 2012, **4**, 4700.

12 M. S. Schmidt, J. Hubner and A. Boisen, *Adv. Mater.*, 2012, **24**, 11.

13 Z. Krpetic, L. Guerrini, I. A. Larmour, J. Reglinski, K. Faulds and D. Graham, *Small*, 2012, **8**, 707.

14 R. A. Alvarez-Puebla and L. M. Liz-Marzan, *Angew. Chem., Int. Ed.*, 2012, **51**, 11214.

15 C. X. Zhang, L. Su, Y. F. Chan, Z. L. Wu, Y. M. Zhao, H. J. Xu and X. M. Sun, *Nanotechnology*, 2013, **24**, 335501.

16 C. Wang, Y. Chen, T. Wang, Z. Ma and Z. Su, *Adv. Funct. Mater.*, 2008, **18**, 355.

17 S. Khatua, P. M. R. Paulo, H. Yuan, A. Gupta, P. Zijlstra and M. Orrit, *ACS Nano*, 2014, **8**, 4440.

18 K. D. Osberg, M. Rycenga, G. R. Bourret, K. A. Brown and C. A. Mirkin, *Adv. Mater.*, 2012, **24**, 6065.

19 A. F. Stewart, A. Lee, A. Ahmed, S. Ip, E. Kumacheva and G. C. Walker, *ACS Nano*, 2014, **8**, 5462.

20 E. Petryayeva and U. J. Krull, *Anal. Chim. Acta*, 2011, **706**, 8.

21 P. Kühler, E.-M. Roller, R. Schreiber, T. Liedl, T. Lohmüller and J. Feldmann, *Nano Lett.*, 2014, **14**, 2914.

22 J. F. Li, S. Y. Ding, Z. L. Yang, M. L. Bai, J. R. Anema, X. Wang, A. Wang, D. Y. Wu, B. Ren, S. M. Hou, T. Wandlowski and Z. Q. Tian, *J. Am. Chem. Soc.*, 2011, **133**, 15922.

23 X. Li, W. C. H. Choy, X. Ren, D. Zhang and H. Lu, *Adv. Funct. Mater.*, 2014, **24**, 3114.

24 Y. K. Kim, S. W. Han and D. H. Min, *ACS Appl. Mater. Interfaces*, 2012, **4**, 6545.

25 J. Han, Y. Dou, M. Wei, D. G. Evans and X. Duan, *Angew. Chem., Int. Ed.*, 2010, **49**, 2171.

26 G. R. Williams and D. O'Hare, *J. Mater. Chem.*, 2006, **16**, 3065.

27 G. R. Williams, A. M. Fogg, J. Sloan, C. Taviot-Gueho and D. O'Hare, *Dalton Trans.*, 2007, 3499.

28 Q. Wang and D. O'Hare, *Chem. Rev.*, 2012, **112**, 4124.

29 L. Desigaux, M. B. Belkacem, P. Richard, J. Cellier, P. Leone, L. Cario, F. Leroux, C. Taviot-Gueho and B. Pitard, *Nano Lett.*, 2006, **6**, 199.

30 F. Leroux and C. Taviot-Guého, *J. Mater. Chem.*, 2005, **15**, 3628.

31 M. Darder, M. López-Blanco, P. Aranda, F. Leroux and E. Ruiz-Hitzky, *Chem. Mater.*, 2005, **17**, 1969.

32 M. Shao, X. Xu, J. Han, J. Zhao, W. Shi, X. Kong, M. Wei, D. G. Evans and X. Duan, *Langmuir*, 2011, **27**, 8233.

33 D. Yan, J. Lu, J. Ma, S. Qin, M. Wei, D. G. Evans and X. Duan, *Angew. Chem., Int. Ed.*, 2011, **50**, 7037.

34 D. Yan, J. Lu, M. Wei, S. Qin, L. Chen, S. Zhang, D. G. Evans and X. Duan, *Adv. Funct. Mater.*, 2011, **21**, 2497.

35 R. Tian, R. Liang, D. Yan, W. Shi, X. Yu, M. Wei, L. S. Li, D. G. Evans and X. Duan, *J. Mater. Chem. C*, 2013, **1**, 5654.

36 W. Shi, S. He, M. Wei, D. G. Evans and X. Duan, *Adv. Funct. Mater.*, 2010, **20**, 3856.

37 S. J. Lee, A. R. Morrill and M. Moskovits, *J. Am. Chem. Soc.*, 2006, **128**, 2200.

38 R. Gunawidjaja, S. Peleshanko, H. Ko and V. V. Tsukruk, *Adv. Mater.*, 2008, **20**, 1544.

39 J. Zhao, X. Kong, W. Shi, M. Shao, J. Han, M. Wei, D. G. Evans and X. Duan, *J. Mater. Chem.*, 2011, **21**, 13926.

40 R. Kenneth, G. Daniel and J. Michael, *Chem. Mater.*, 2000, **12**, 306.

41 R. Liang, S. Xu, D. Yan, W. Shi, R. Tian, H. Yan, M. Wei, D. G. Evans and X. Duan, *Adv. Funct. Mater.*, 2012, **22**, 4940.

42 X. Li, W. C. H. Choy, X. Ren, D. Zhang and H. Lu, *Adv. Funct. Mater.*, 2014, **24**, 3114.

43 L.-Y. Chen, K.-H. Yang, H.-C. Chen, Y.-C. Liu, C.-H. Chen and Q.-Y. Chen, *Analyst*, 2014, **139**, 1929.

44 S. Kundu, *J. Mater. Chem. C*, 2013, **1**, 831.

45 S. Su, C. Zhang, L. Yuwen, J. Chao, X. Zuo, X. Liu, C. Song, C. Fan and L. Wang, *ACS Appl. Mater. Interfaces*, 2014, **6**, 18375.

46 L. Zhang, H. Ma and L. Yang, *RSC Adv.*, 2014, **4**, 45207.

47 Z.-Q. Tian, B. Ren, J.-F. Li and Z.-L. Yang, *Chem. Commun.*, 2007, 3514.

48 D. A. Genov, A. K. Sarychev, V. M. Shalaev and A. Wei, *Nano Lett.*, 2004, **4**, 153.

49 K. L. Kelly, E. Coronado, L. L. Zhao and G. C. Schatz, *J. Phys. Chem. B*, 2003, **107**, 668.

50 H. Xu, J. Aizpurua, M. Kall and P. Apell, *Phys. Rev. E: Stat., Nonlinear, Soft Matter Phys.*, 2000, 4318.

51 X. Wang, M. Li, L. Meng, K. Lin, J. Feng, T. Huang, Z. Yang and B. Ren, *ACS Nano*, 2014, **8**, 528.

52 Y. Aharonov, S. Massar, S. Popescu, J. Tollaksen and L. Vaidman, *Phys. Rev. Lett.*, 1996, **77**, 1163.

53 M. Y. Lv, H. Y. Teng, Z. Y. Chen, Y. M. Zhao, X. Zhang, L. Liu, Z. Wu, L. M. Liu and H. J. Xu, *Sens. Actuators, B*, 2015, **209**, 820.

54 R. F. Aroca, *Phys. Chem. Chem. Phys.*, 2013, **15**, 5355.

55 Y. He, S. Su, T. Xu, Y. Zhong, J. A. Zapien, J. Li, C. Fan and S.-T. Lee, *Nano Today*, 2011, **6**, 122.

56 H. J. Yin, Y. F. Chan, Z. L. Wu and H. J. Xu, *Opt. Lett.*, 2014, **39**, 4184.

57 L.-Y. Chen, K.-H. Yang, H.-C. Chen, Y.-C. Liu, C.-H. Chen and Q.-Y. Chen, *Analyst*, 2014, **139**, 1929.

58 X. Chen, C. Jiang and S. Yu, *CrystEngComm*, 2014, **16**, 9959.

59 B. Saute, R. Premasiri, L. Ziegler and R. Narayanan, *Analyst*, 2012, **137**, 5082.

60 X. Tang, W. Cai, L. Yang and J. Liu, *Nanoscale*, 2013, **5**, 11193.

61 Y. Zhang, Z. Wang, L. Wu, Y. Pei, P. Chen and Y. Cui, *Analyst*, 2014, **139**, 5148.

62 B. Han, N. Choi, K. H. Kim, D. W. Lim and J. Choo, *J. Phys. Chem. C*, 2011, **115**, 6290.

63 L. He, N.-J. Kim, H. Li, Z. Hu and M. Lin, *J. Agric. Food Chem.*, 2008, **56**, 9843.

64 L.-B. Zhong, J. Yin, Y.-M. Zheng, Q. Liu, X.-X. Cheng and F.-H. Luo, *Anal. Chem.*, 2014, **86**, 6262.

65 S. Lee, J. Choi, L. Chen, B. Park, J. B. Kyong, G. H. Seong, J. Choo, Y. Lee, K.-H. Shin, E. K. Lee, S.-W. Joo and K.-H. Lee, *Anal. Chim. Acta*, 2007, **590**, 139.

66 Z. Li, J. Lu, S. Li, S. Qin and Y. Qin, *Adv. Mater.*, 2012, **24**, 6053.

67 Y. Qin, J. Lu, S. Li, Z. Li and S. Zheng, *J. Phys. Chem. C*, 2014, **118**, 20538.

68 S. Srivastava, V. Ball, P. Podsiadlo, J. Lee, P. Ho and N. A. Kotov, *J. Am. Chem. Soc.*, 2008, **130**, 3748.

69 D. S. Salloum and J. B. Schlenoff, *Biomacromolecules*, 2004, **5**, 1089.

70 N. Hoda and R. G. Larson, *J. Phys. Chem. B*, 2009, **113**, 4232.

71 X. Zhang and Z. Su, *Adv. Mater.*, 2012, **24**, 4574.

72 W. Shi, Y. Lin, X. Kong, S. Zhang, Y. Jia, M. Wei, D. G. Evans and X. Duan, *J. Mater. Chem.*, 2011, **21**, 6088.